THE ASTROPHYSICAL JOURNAL, 467:794–805, 1996 August 20

ANALYZING X-RAY PULSAR PROFILES: GEOMETRY AND BEAM PATTERN OF CENTAURUS X-3

U. KRAUS, S. BLUM, J. SCHULTE, AND H. RUDER
Universität Tübingen, Institut für Astronomie und Astrophysik, Auf der Morgenstelle 10C, 72076 Tübingen, Germany;
kraus,blum,schulte,
ruder@tat.physik.uni-tuebingen.de

AND

P. MÉSZÁROS
Pennsylvania State University, 525 Davey Lab, University Park, PA 16802; nnp@astro.psu.edu
Received 1995 September 25; accepted 1996 March 5

ABSTRACT

We present an analysis of the energy-dependent asymmetric pulse profile of the X-ray pulsar Cen X-3. We show that the data are compatible with the assumption that the asymmetry is caused by a distorted magnetic dipole field. Based on this assumption, it is possible to decompose the pulse profile into the contributions of the two emission regions at the magnetic poles. The results of the decomposition indicate that Cen X-3 has two equal emission regions which are displaced from antipodal positions by approximately 10° and have a pencil plus fan beam pattern.

Subject headings: pulsars: individual (Centaurus X-3) — stars: individual (Centaurus X-3) — X-rays: stars

1. INTRODUCTION

The observation of regular 4.8s X-ray pulsations from Centaurus X-3 in 1971 (Giacconi et al. 1971) was the first discovery of a binary X-ray pulsar. This X-ray source is now understood to be an accreting neutron star in a binary system orbiting its O-type supergiant companion V778 Cen every 2.1 days while rotating with a period of 4.8 s.

Cen X-3 is one of six out of about 35 X-ray pulsars known today in which the observation of X-ray eclipses has permitted the determination of all orbital and stellar parameters. In particular, the inclination of the orbital plane and the mass of the neutron star have been estimated by Joss & Rappaport (1984) to be $i > 63°$, $M = 1.07^{+0.63}_{0.57}$ $M_\odot$ and by Nagase (1989) to be $i = 75°^{+12}_{-13}$, $M = 1.06^{+0.56}_{-0.53}$ $M_\odot$.

The luminosity of Cen X-3 has been reported to alternate between extended high states and low states on a timescale of months (Schreier et al. 1976; Priedhorsky & Terrell 1983). For an assumed distance of 8 kpc, the high-state luminosity is $L = 10^{31}$ W, which makes Cen X-3 one of the most luminous binary pulsars known.

The pulse profile usually shows a single peak with a sharp rise and a more gradual decline ending in a shoulder that is most prominent at low energies (Ulmer 1976; van der Klis, Bonnet-Bidaud, & Robba 1980; White, Swank, & Holt 1983; Howe et al. 1983; Lieu, Vankatesan, & Mitani 1984). On several occasions, a double-peaked pulse profile has been detected at low energies (Schreier et al. 1976; Tuohy 1976; Dolan et al. 1984; Nagase et al. 1992). The single-peaked pulse profile is strongly asymmetric, the double-peaked one moderately so.

Several analyses of the pulse profile of Cen X-3 have been carried out with the purpose to determine geometry and beam pattern from the pulse shape. Wang & Welter (1981) were able to reproduce the low-energy single-peak pulse profile with a phenomenological parameterized asymmetric fan beam pattern. Leahy (1991) modeled the polar emission regions as rings or caps which can be offset from antipodal positions on the neutron star. A good fit to the medium-energy single-peak pulse profile required large caps with a considerable offset. The polar cap model was taken up by Riffert et al. (1993) and extended to include relativistic light deflection, with the result that the required ring size and offset were greatly reduced. In the fan beam model of Wang & Welter, asymmetry is inherent to the beam pattern of the emission regions. In the polar cap model used by Leahy and Riffert et al., the emission regions are axisymmetric, and asymmetry is introduced by means of their nonantipodal location. In order that there are two nonantipodal magnetic poles, the magnetic dipole field that is usually assumed for the neutron star has to be somewhat distorted. Distorted dipole models have also been used in analyses of pulse profiles and spectra of other X-ray pulsars (Bulik et al. 1992, 1995; Parmar, White, & Stella 1989).

The assumption that the asymmetry in the pulse profiles of X-ray pulsars is predominantly due to a distorted dipole geometry may seem plausible by the following consideration. In principle, a somewhat asymmetric accretion stream should produce an asymmetric beam pattern and so cause an intrinsic asymmetry. Model calculations indicate, however, that the corresponding asymmetry of the beam pattern may well be very small (Basko & Sunyaev 1975), in fact too small to explain the prominent asymmetry seen in many pulse profiles. On the other hand, asymmetric pulse profiles arise naturally in a distorted dipole geometry, since even moderate displacements of the emission regions from the antipodal positions can be sufficient to produce appreciable asymmetry.

In this paper, we address the question if the energy-dependent pulse profile of Cen X-3 is compatible with the assumption that its asymmetry is purely due to a distorted dipole geometry. We analyze a total of 17 pulse profiles including both single-peaked and double-peaked pulse profiles (White et al. 1983; Nagase et al. 1992; Nagase 1989; Kunz 1994). We find that the data on Cen X-3 are indeed compatible with the assumption that the asymmetry is caused by a distorted dipole geometry. Adopting this assumption, we obtain a decomposition of the pulse profile

into the contributions of the two emission regions. We show then that the contributions of the two emission regions indicate that there are two equal emission regions in Cen X-3 (i.e., that the beam patterns of the two emission regions are identical). This fact is exploited to reconstruct the visible part of the beam pattern, to determine the pulsar geometry, and to obtain an approximation to the local emission pattern of the emission regions.

The analysis presented here is an application of the new model-independent method of analyzing pulse profiles described by Kraus et al. (1995). Unlike the analyses mentioned above, this approach does not involve assumptions about the local emission pattern or the beam pattern of the emission regions. Instead, we start with the observed pulse profile and work backward toward the beam pattern and the geometry, relying on symmetry properties present in the data. Also, to our knowledge this is the first analysis of the pulse profiles of Cen X-3 that takes the energy dependence and the long-term variability of the pulse profile into account. A short summary of the method is given in § 2. In § 3 we discuss the data used in this analysis, and in § 4 we argue that they are compatible with the assumption of nonantipodal emission regions with axisymmetric beam patterns, and deduce first the single-pole contributions and then geometry and beam pattern. A discussion of the remaining ambiguities in the decomposition and an interpretation of the beam pattern in terms of angle-dependent spectra, intrinsic beam pattern, and constraints on the size of the emission region are given in § 5.

2. THE METHOD

This section is a short summary of the method that we use to analyze the energy dependent pulse profile of Cen X-3. For details, see Kraus et al. (1995).

2.1. *Decomposition into Single-Pole Pulse Profiles*

The observed pulse profile is the sum of the contributions of the two emission regions near the magnetic poles $F(\Phi) = f_1(\Phi) + f_2(\Phi)$. We decompose F into f_1 and f_2 under the assumption that (i) the single-pole pulse profiles are symmetric because the beam patterns of the emission regions are axisymmetric, i.e., are functions only of the angle θ between the magnetic axis and the direction of observation, and (ii) the emission regions are not antipodal, so that the symmetry points of the two symmetric functions do not coincide.

Formally, a decomposition into two symmetric functions exists for virtually every choice of their symmetry points Φ_1 and Φ_2. With $\Delta := \pi - (\Phi_1 - \Phi_2)$, the parameter space of all possible formal decompositions is $0 \le \Phi_1 \le \pi$, $0 \le \Delta \le \pi/2$. We search the Φ_1-Δ space for decompositions that satisfy the conditions that the symmetric functions are (i) both positive, (ii) simple and smooth, and (iii) smoothly dependent on energy.

2.2. *Search for an Overlap Region and Determination of the Geometry*

In the course of one revolution of the neutron star, the viewing angle θ onto emission region k varies over some range $\theta_{k,\,\min} \le \theta \le \theta_{k,\,\max}$. Depending on the pulsar geometry, the θ ranges of the two emission regions may overlap. If the two emission regions have identical beam patterns, then an overlap in the θ ranges translates into an overlap in the two symmetric functions. In order to search for this overlap region, the symmetric functions are transformed into functions of a common variable q through $\cos(\Phi - \Phi_1) = q$ for f_1 and $\cos(\Phi - \Phi_2) = (q - a)/b$ for f_2. The real numbers a and $b > 0$ are determined by means of a fit which minimizes the quadratic deviation between $f_1(q)$ and $f_2(q)$ in the overlap region.

From the values of a, b, and Δ, we determine the pulsar geometry under the assumption that the rotation axis of the neutron star is perpendicular to the orbital plane, so that the angle Θ_O between the direction of observation and the rotation axis of the neutron star is given by the inclination of the orbital plane.

3. THE DATA

A total of 17 pulse profiles, observed by the *Ginga* (Nagase et al. 1992), *OSO 8* (White et al. 1983), and *Tenma* (Nagase 1989) satellites and the MIR-HEXE detector (Kunz 1994), have been examined. The mentioned pulse profiles were taken from the literature except the latter that have been kindly made available to us by M. Kunz.

It is assumed for all examined pulse profiles that background has been correctly subtracted. Because no information was available about the absolute measured fluxes, the pulse profiles were normalized to have a maximum value of unity.

Since the pulse profiles observed by the different instruments are not phase correlated, we had to align their phases in order to compare the results of the calculations. To do so, the *Ginga* pulse profiles were taken as a reference. From each of the other observations, the pulse profile that has the most similar shape compared with one of the *Ginga* pulse profiles was picked out and shifted in phase until the main peak was in phase with that of the corresponding *Ginga* observation. Then the same phase shift was added to all the other pulse profiles of this observation.

Finally, the data were smoothed by regarding only a certain number of Fourier coefficients that are sufficient to reproduce the features of the observed pulse profiles. Because of the small statistical error of the *Ginga* data, we used all 32 Fourier coefficients. On the other hand, we smoothed the *OSO 8* data by omitting the highest Fourier coefficients with large relative statistical errors. For the O2 and O3 pulse profiles, we considered the lower 32 and for

TABLE 1

PULSE PROFILES AND THEIR RESPECTIVE ENERGY RANGES

Pulse Profile	Energy Range (keV)
OSO 8 (60 Phase Bins)	
O1	1.0–2.3
O2	2.3–8.3
O3	8.3–12.5
O4	12.5–25.0
Ginga (32 Phase Bins)	
G1	1.2–2.3
G2	2.3–4.8
G3	4.8–6.9
G4	6.9–9.3
G5	9.3–13.9
G6	13.9–18.5
G7	18.5–27.8

NOTE.—Pulse profiles are shown in Fig. 1.

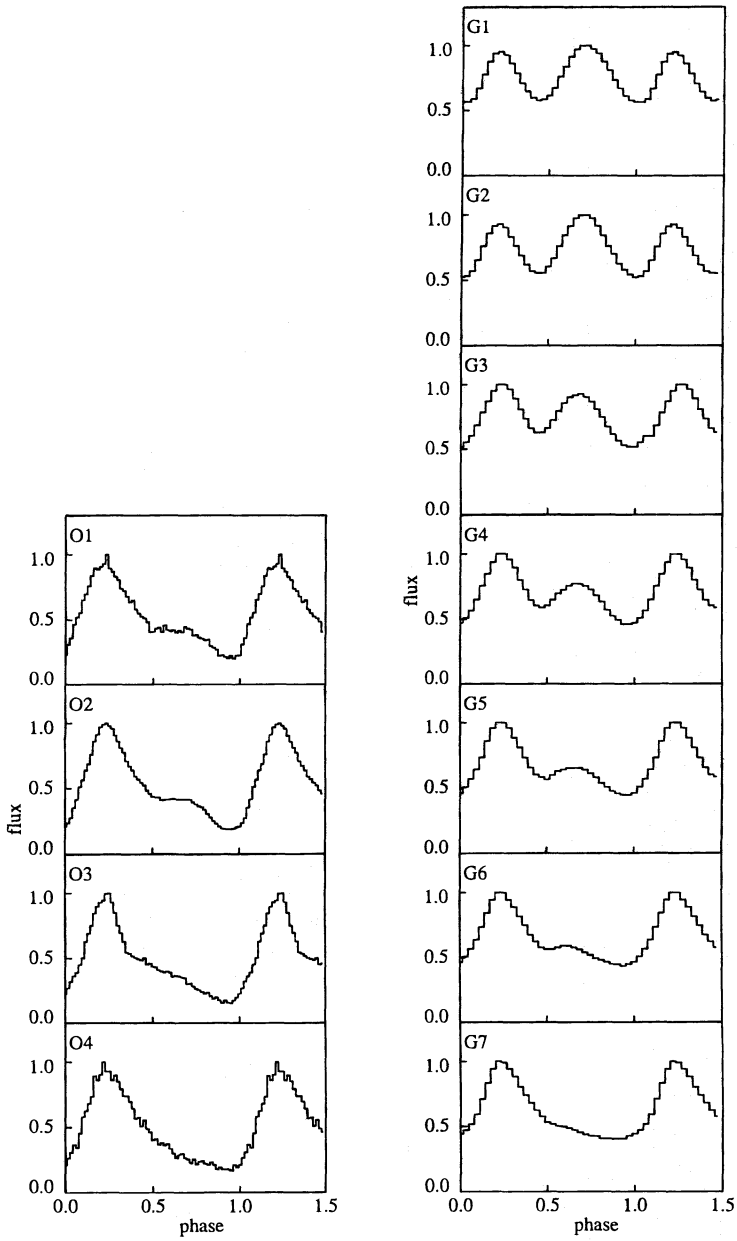

FIG. 1.—Pulse profiles of Cen X-3 observed with the *OSO 8* (*left*) and the *Ginga* satellites (*right*). The data are taken from White et al. (1983) and Nagase et al. (1992). See also Table 1.

the O1 and O4 pulse profiles the lower 20 Fourier coefficients.

The *OSO 8* data have a good time resolution, and the statistical error of the *Ginga* data is very small. In this section, therefore we will first examine the 11 pulse profiles of these two observations; the others will be discussed in § 5. Originally, Nagase et al. (1992) published two more pulse profiles than the seven listed in Table 1. We omitted one pulse profile in the energy range 27.8–37 keV because it contains a dip that is only two phase bins wide and is therefore presumably undersampled. Two pulse profiles in the energy ranges 9.3–11.6 and 11.6–13.9 keV seem to be identical, so we combined them.

Having a look at the observed pulse profiles in Figure 1, we analyze both the typical Cen X-3 pulse profile with a single peak and a shoulder (as observed by *OSO 8* and by *Ginga* at higher photon energy) and the double-peaked pulse profiles found by *Ginga* at low photon energy.

4. RESULTS

4.1. *Decomposition into Single-Pole Pulse Profiles*

The nonnegative criterion has been applied to all pulse profiles simultaneously, with the result shown in Figure 2. Each point in the Φ_1-Δ parameter space corresponds to a formal decomposition of each of the 11 pulse profiles into two symmetric functions.

A decomposition is rejected if one or more of the 2×11 symmetric functions have negative values. This eliminates the entire parameter space outside the boundary curve, shown as a dashed line. According to Figure 2, nonnegative decompositions are obtained for $\Phi_1 \approx 70°$–$90°$ with a large range of values of $\Delta(20° \leq \Delta \leq 90°)$. Since rotation angle $\Phi_1 = 90°$ corresponds to phase 0.25, these are decompositions for which one of the symmetry points of symmetric function 1 is close to the phase of the main peak of the observed pulse profile. There is a second smaller region with

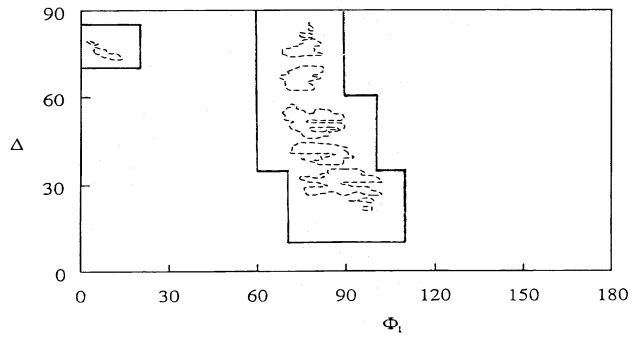

FIG. 2.—The nonnegative criterion: outside the boundary curve (*dashed line*) the decomposition of all the pulse profiles into symmetric functions gives at least one symmetric function with negative values. For reasons mentioned in the text, a somewhat larger region (*solid line*) is used in the search for acceptable decompositions.

nonnegative decompositions at $\Phi_1 \approx 10°$, $\Delta \approx 75°$. In this case, neither of the symmetry points of symmetric function 1 is close to the main peak of the observed pulse profile, but one of the symmetry points of symmetric function 2 is, since it follows from the definition of Δ that $\Phi_2 + 180° = \Delta + \Phi_1 \approx 85°$. Thus, we find that nonnegative decompositions require that one of the symmetric functions have its symmetry point close to the phase of the main peak of the observed pulse profile. A possible source of error for the boundary curve is an inaccurate alignment of the phases of pulse profiles from different observations. For this reason, the finer details of the boundary curve are not meaningful, and we retain a somewhat larger region around it (solid line in Fig. 2), which we search for decompositions that are nonnegative and in addition both simple and smooth.

Since the observed pulse profiles show one or two peaks per pulse period and we do not expect the single-pole pulse profiles to be considerably more complicated than the observed pulse profiles, we call a decomposition simple if the symmetric functions have at most two peaks per pulse period. A decomposition is considered smooth if prominent ripples are absent. In general, the symmetric functions will be less smooth than the pertinent observed pulse profile because the statistical error increases somewhat in the decomposition. Other than being simple and smooth, we expect the single-pole pulse profiles to show an energy dependence as gradual as that of the observed pulse profiles.

The result of the search for acceptable decompositions is shown in Figure 3. Each plot shows the pair of symmetric functions obtained for the pulse profile specified in the header. Since the distribution of the unmodulated flux among the two symmetric functions cannot be determined in the decomposition, the minima of the symmetric functions are shifted to zero, and the remaining unmodulated flux is indicated by the horizontal line at the left-hand side of the plot. The sum of the two symmetric functions plus the remaining unmodulated flux reproduces exactly the respective observed pulse profile. The parameters Φ_1 and Δ of each decomposition are given in the header. There is some variation in the decomposition parameters, with Φ_1 in the range $87° \leq \Phi_1 \leq 100°$ and Δ in the range $26° \leq \Delta \leq 39°$. The same parameters cannot be used for all the plots because the smoothness of the symmetric functions may vary quickly with Φ_1 and Δ on a small scale, especially if the number of Fourier coefficients is large. On the other hand, once the smooth decompositions have been picked out, their shape varies gradually with the parameters. In general, because of the limited resolution of the pulse profiles in rotation angle (the bin width is 11°.25 for the *Ginga* data) and the additional uncertainty in the alignment of the phases of pulse profiles from different observations, we do not attempt to determine Φ_1 and Δ to do better than about 12°–15°, i.e., we search for a square of 15° × 15° in the parameter plane which contains acceptable decompositions of all pulse profiles. The symmetric functions shown in Figure 3 meet all the criteria listed above, i.e., smoothness, simple shape, and gradual energy dependence, so that we can conclude that the asymmetric pulse profile of Cen X-3 can be understood in terms of two symmetric single-pole pulse profiles from nonantipodal emission regions.

Of course, the decomposition of each observed pulse profile that is shown in Figure 3 is not the only acceptable decomposition of that pulse profile. Rather, this decomposition is a representative for a certain region in the Φ_1-Δ parameter space which contains a large number of acceptable decompositions that are qualitatively very similar. The size of this region and the variation of the decomposition within it as well as the reasons for choosing this particular set of representatives will be discussed in § 5.

4.2. *Search for an Overlap Region and Determination of the Geometry*

The single-pole pulse profiles shown above were transformed into functions of the auxiliary variable q. Since an overlap region appeared to exist, best-fit values of the parameters a and b were determined. Figure 4 shows the single-pole pulse profiles as functions of q with the best-fit values $a = -1.5$ and $b = 0.95$. Consider, e.g., panel O1 in Figure 4. The function on the right-hand side that is defined for $-1 \leq q \leq 1$ and drawn with a solid line stems from the symmetric single-pole pulse profile drawn with a solid line in panel O1 in Figure 3. This single-pole pulse profile was transformed into a function of q via $\cos(\Phi - \Phi_1) = q$. The point $q = 1$ corresponds to the symmetry point at the peak of the higher maximum at phase 0.275, and the point $q = -1$ corresponds to the peak of the smaller maximum at phase 0.775. The function on the left-hand side that is defined for $-2.5 \leq q \leq -0.6$ and drawn with a dashed line is obtained from the other symmetric single-pole pulse profile in panel O1 of Figure 3, drawn there as a dashed line also. Here $q = -0.6$ corresponds to the symmetry point in the minimum at phase 0.88 and $q = -2.5$ corresponds to the minimum at phase 0.38. The transformation is $\cos(\Phi - \Phi_2) = (q - a)/b$, where a and b have been adjusted to mimimise the quadratic deviation of the two functions in the overlap region. For the best-fit values of a and b given above, the overlap region turns out to be $-1 \leq q \leq -0.6$.

Figure 4 shows that each pair of functions joins smoothly in the best-fit overlap region. The overlapping parts of the functions are approximately linear in all cases, but with different slopes. When dealing with one pair of functions at a time, the parameter b can obviously be adjusted to bring the slopes into agreement and the parameter a to make the functions coincide. The evidence of Figure 4 is that the same values of a and b work for all pairs of functions, even though the slopes themselves differ.

This evidence indicates that Cen X-3 probably has two emission regions with the same beam pattern: When transformed into a function of q, each single-pole pulse profile is

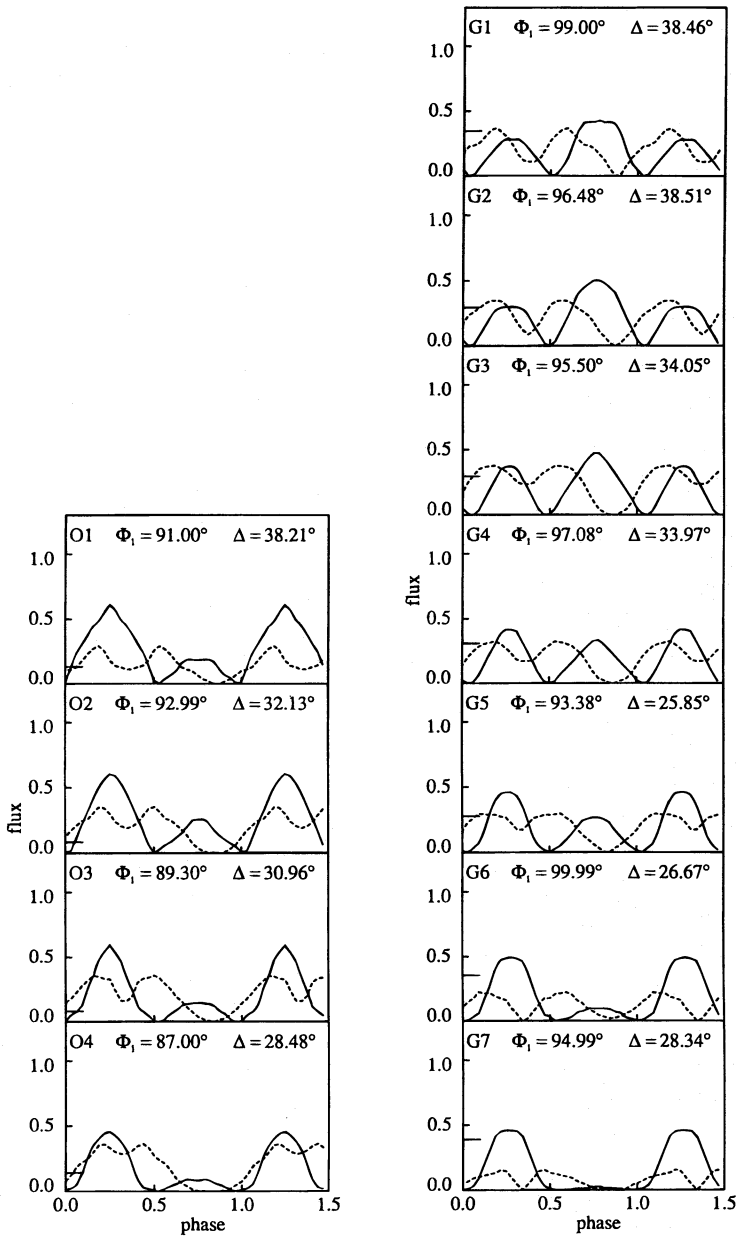

FIG. 3.—Decompositions of the analyzed pulse profiles into two symmetric single-pole pulse profiles. The header of each plot gives the decomposition parameters Φ_1 and Δ and identifies the decomposed pulse profile. Since the distribution of the unmodulated flux among the two symmetric functions cannot be determined in the decomposition, the minima of the symmetric functions are shifted to zero, and the remaining unmodulated flux is indicated by the horizontal line at the left-hand side of the plot.

a section of the (suitably transformed) beam pattern of the emission region that it originates from. In § 2, we argued that in the case of two emission regions with the same beam pattern there may be a part of the beam pattern that shows up in both single-pole pulse profiles. According to Figure 4, such a region common to both single-pole pulse profiles exists in the case of Cen X-3. We conclude that the composite functions in Figure 4 represent the common energy dependent beam pattern of the two emission regions as a function of q.

The location of the magnetic poles on the neutron star surface can be described by means of their polar angles Θ_1 and Θ_2 with respect to the rotation axis and by the angular distance δ between the location of the second magnetic pole and the point that is antipodal to the first magnetic pole (see Fig. 5). Figure 6 illustrates the constraints on the pulsar geometry that follow from the values determined for Δ, a, and b: Θ_1, Θ_2, and δ can all be expressed as functions of the unknown angle Θ_o between the direction of observation and the rotation axis. The solid lines are obtained for the best-fit values $a = -1.5$ and $b = 0.95$ of Figure 4. The constraint $\delta(\Theta_o)$ depends on Δ as well as on a and b. Since there is some variation in Δ among the decompositions of Figure 3, we plot one curve for each value of Δ. As was mentioned above and will be discussed in § 5, there is some arbitrariness in the choice of representative decompositions. The dashed lines in Figure 6 are obtained for another set of decompositions within the Φ_1-Δ region that the decompositions of Figure 3 represent and indicate the extent of uncertainty in the geometry on this account. If we assume that the rotation axis of the neutron star is perpendicular to the orbital plane, then the direction of observation Θ_o is equal

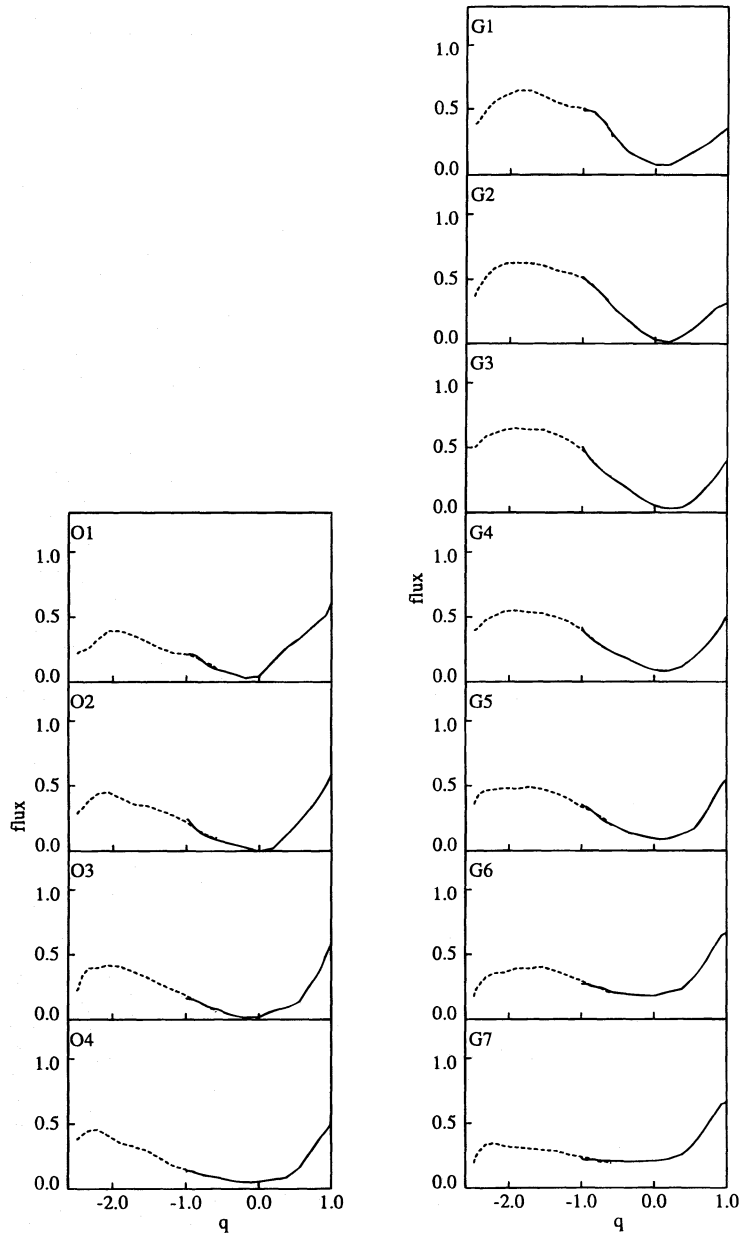

FIG. 4.—Single-pole pulse profiles as functions of the auxiliary variable q using the best-fit values $a = -1.5$ and $b = 0.95$. An overlap region exists and covers the range $-1.0 \leq q \leq -0.6$.

to the orbital inclination $i = 75^{\circ}{}^{+12}_{-13}$ (Nagase 1989). In Figure 6, $i = 75^{\circ}$ is marked by the solid vertical line, and the error range is marked by the two dashed vertical lines. With $\Delta = 32.75$ (the arithmetic means of the Δ parameters of Fig. 3), a and b as above, and $\Theta_o = 75^{\circ}$, we obtain $\Theta_1 = 18^{\circ}$, $\Theta_2 = 161^{\circ}$, and $\delta = 10^{\circ}$. The uncertainty in these values is due mainly to the large uncertainty in i and therefore is roughly of the same magnitude as the latter. Note the small value obtained for δ: the two magnetic poles are only slightly offset from antipodal positions on the neutron star surface. This shows that a fairly small distortion of the magnetic dipole field is sufficient to explain the considerable asymmetry of the pulse profiles of Cen X-3.

Finally, we obtain the beam pattern as a function of θ by using the geometric parameters given above to relate θ and the auxiliary variable q. This relation is of the general form $\cos(\theta) = \pm F(q, \Theta_1, \Theta_2, \delta, \Theta_o)$. Within this analysis, it is not possible to decide if the plus or the minus sign is the correct choice. Both solutions are shown in Figure 7 where the lower abscissa gives the θ-values of the "plus" solution and the upper abscissa gives those of the "minus" solution.

The beam pattern was reconstructed in the range $56^{\circ} \leq \theta \leq 123^{\circ}$ ("plus" solution) or $57^{\circ} \leq \theta \leq 124^{\circ}$ ("minus" solution). There is no information about $\theta < 56^{\circ}$ or about $\theta < 57^{\circ}$, respectively, because during the rotation of the neutron star, neither of the magnetic axes of the two poles comes as close as this to the direction of observation. This applies analogously to $\theta > 123^{\circ}$ ("plus" solution) and $\theta > 124^{\circ}$ ("minus" solution).

The general structure of the beam pattern is that of a peak at small θ_- and a rise toward large θ_-. The relative size of the peak and the rising part changes with the photon energy from a dominant peak at low energy (G1) to a dominant rise at high energy (G7). The positions of the peak at $\theta_- \approx 70^{\circ}$ and of the minimum between peak and rise at $\theta_- \approx 105^{\circ}$ are independent of photon energy.

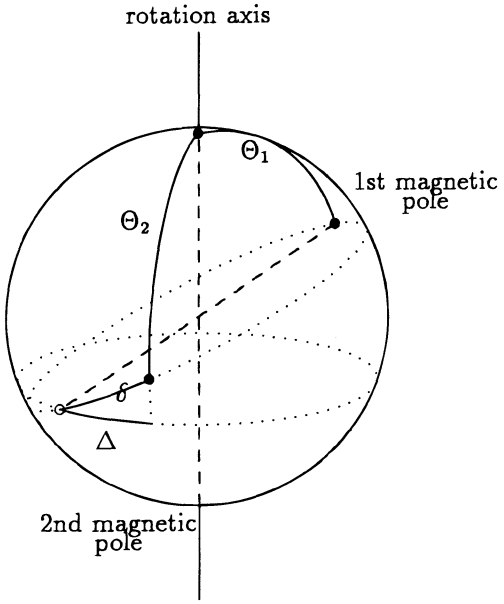

FIG. 5.—The intrinsic pulsar geometry: the locations of the magnetic poles on the neutron star surface can be described by means of their polar angles Θ_1 and Θ_2 with respect to the rotation axis and by the angular distance δ between the location of the second magnetic pole and the point that is antipodal to the first magnetic pole. Here Δ is the difference in longitude between the actual and the antipodal position of the second magnetic pole, again with respect to the rotation axis.

5. DISCUSSION

5.1. *Acceptable Decompositions*

The decompositions shown in Figure 3 display a gradual energy dependence which preserves the basic features of the single-pole pulse profiles: One of them, drawn as a solid line in Figure 3, has two peaks per pulse period with different heights; the other one, drawn as a dashed line in Figure 3, has one broad maximum with a more or less shallow depression in the middle.

The region in the Φ_1-Δ parameter space in which the acceptable decompositions are of this type is approximately $85° \leq \Phi \leq 105°$, $10° \leq \Delta \leq 40°$. There is a certain amount of variation in the decompositions of any given pulse profile within this solution region. Figure 8 illustrates the typical extent of the variation using pulse profile G3 as an example.

The set of representatives shown in Figure 3 comprises decompositions with $25° \leq \Delta \leq 39°$, i.e., decompositions located in the "high-Δ" part of the solution region. With regard only to the decomposition, one might just as well choose a set of representatives in the "low-Δ" ($10° \leq \Delta \leq 25°$) part. The typical difference between high-Δ and low-Δ decompositions is illustrated in Figure 9 using again pulse profile G3 as an example. The decomposition with $\Delta = 34°$ and the resulting combined pulse profiles as a function of q (*top row*) are taken from Figures 3 and 4, respectively. The decomposition with $\Delta = 24°$ (*bottom row*) is more strongly modulated and therefore has less unmodulated flux (indicated by the horizontal lines on the left-hand sides of the plots). As a consequence, the best overlap in the resulting combined function of q makes the minimum of the function drop below zero. If the function is constrained to be positive, no good overlap is obtained. Thus, within the solution region only the decompositions with higher values of Δ are compatible with an interpretation in terms of two identical emission regions and a pulsar geometry that makes the single-pole pulse profiles overlap. The decompositions at lower values of Δ would only be compatible with this scenario if there was more unmodulated flux in the observed pulse profile.

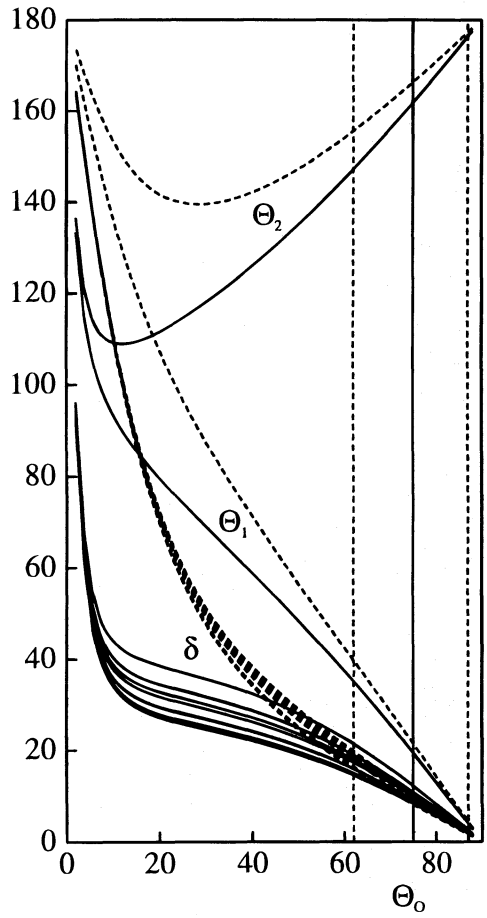

FIG. 6.—The constraints on the pulsar geometry: Θ_1, Θ_2, and δ as functions of the angle Θ_o between the direction of observation and the rotation axis of the neutron star. The solid lines are obtained for the best-fit values $a = -1.5$, $b = 0.95$ of Fig. 4 and the Δ parameters of the decompositions in Fig. 3. The dashed lines result from another set of decompositions to be discussed in § 5. The vertical lines mark the orbital inclination $i = 75°^{+12}_{-13}$ (Nagase 1989) and its error range.

The dashed lines in Figure 6 indicate the constraints on pulsar geometry that would be obtained from a set of low-Δ decompositions for which a good overlap has been obtained at the price of small negative sections of the combined functions of q. As mentioned in § 4, the uncertainty in the determination of the positions of the magnetic poles is due mainly to the uncertainty in the inclination, whereas the difference between constraints from high-Δ and low-Δ decompositions is not crucial.

A search for simple and smooth decompositions has been performed in all parts of the Φ_1-Δ parameter space which are permitted by the nonnegative criterion (Fig. 2). The solution region described above is the lower end of the permitted region. There is one other spot in which acceptable decompositions of all pulse profiles exist that are comparable to those shown in Figure 3 in terms of smoothness, simple shape, and gradual energy dependence. This region is around $60° \leq \Phi_1 \leq 80°$, $75° \leq \Delta \leq 90°$. Figure 10 shows the decomposition of pulse profile G3, which exhibits the characteristics common to the decompositions of all pulse

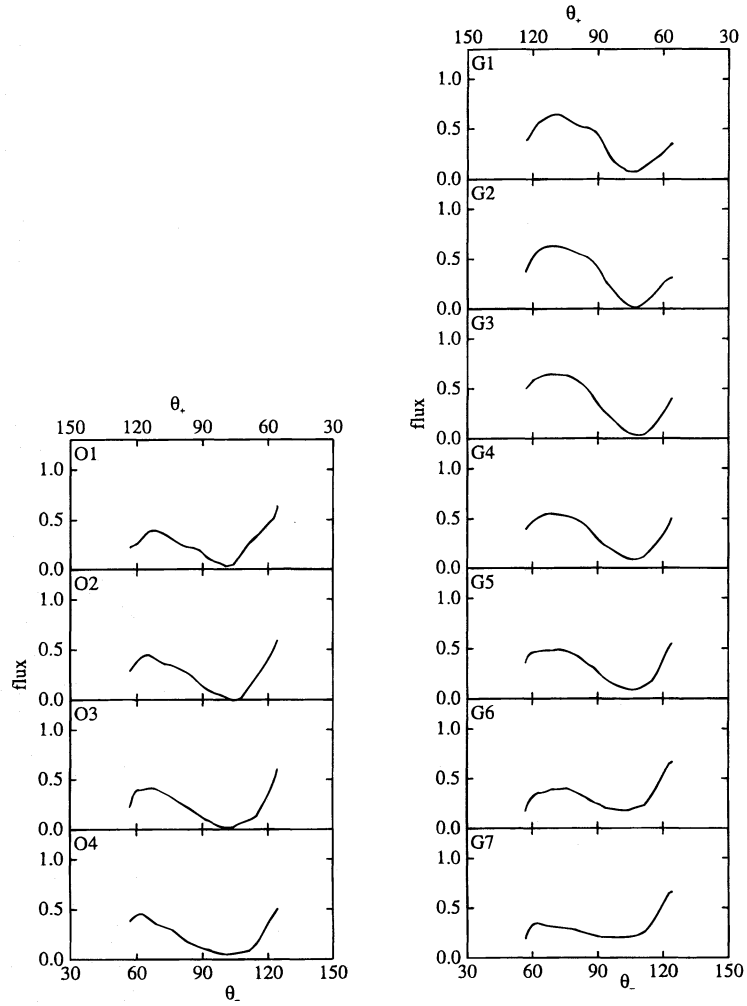

FIG. 7.—Reconstructed energy-dependent beam pattern as a function of the angle θ between the direction of observation and the magnetic axis. The header of each plot identifies the respective pulse profile. Because of the ambiguity present in the relation between q and θ, there are two possible solutions. Both are shown here, the lower abscissa giving the θ-values of the "minus" solution and the upper abscissa giving those of the "plus" solution.

profiles in this region of the parameter space. Here the single-pole pulse profiles have two maxima of different heights each, are strongly modulated, and oscillate in opposition to each other. This decomposition is not compatible with two identical emission regions and a pulsar geometry that makes the single-pole pulse profiles overlap.

Comparing these results with the preliminary results obtained in Kraus et al. (1995) from the analysis of just one pulse profile, we note that the energy dependence of the pulse profile provides a strong constraint and reduces greatly the number of different types of acceptable decompositions.

5.2. *Other Observations of Cen X-3*

In an attempt to extend the results to higher X-ray energies, we analyzed pulse profiles obtained with the MIR-

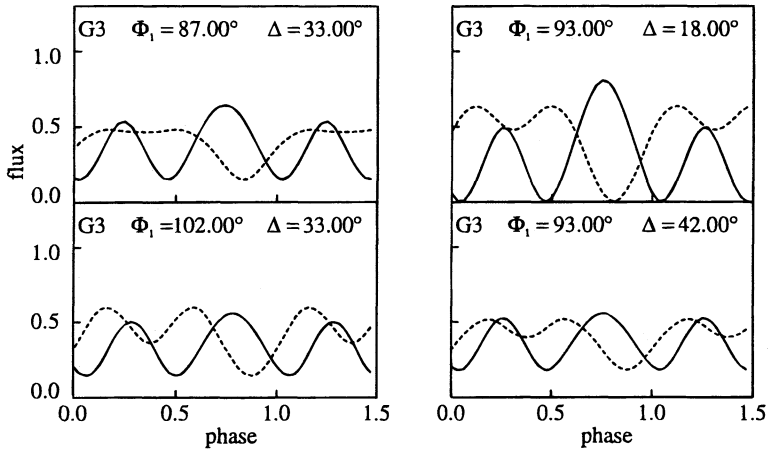

FIG. 8.—Decompositions of pulse profile G3 at four neighboring points in the Φ_1-Δ parameter space. These are acceptable decompositions which are of the same type as the decompositions shown in Fig. 3. They illustrate the extent of variation in the decompositions of this type.

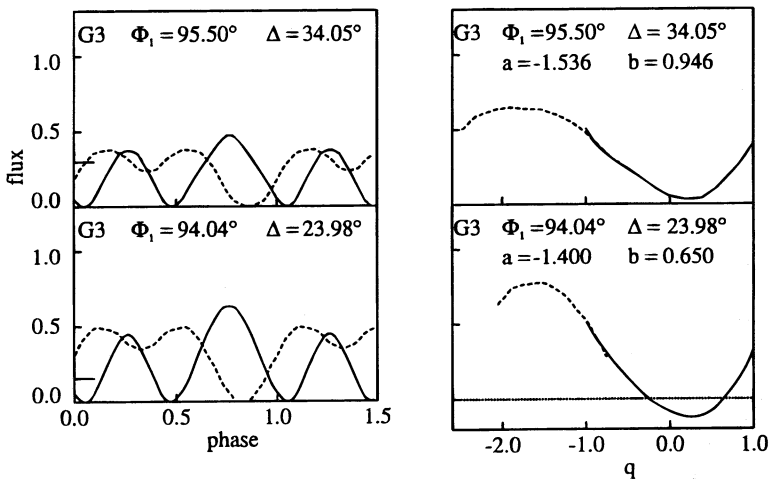

FIG. 9.—Comparison between a "high-Δ" and a "low-Δ" decomposition using pulse profile G3 as an example. The decomposition with Δ = 34° and its combined single-pole pulse profiles as a function of q (*top row*) are taken from Figs. 3 and 4, respectively. The decomposition with Δ = 24° (*bottom row*) is more strongly modulated (there is less unmodulated flux as indicated by the horizontal line at the left-hand side of the plot), and the best overlap in the resulting combined function of q makes the minimum of the function drop below zero. If the function is constrained to be positive, no good overlap is obtained.

HEXE in 1989 June and 1992 January in five energy channels (10–18 keV,18–24 keV, 24–30 keV, 30–50 keV, and 16–30 keV) (Kunz 1994). This analysis was performed independently of the analysis of the *OSO 8* and the *Ginga* data and gave values of Δ, a, and b that are in very good agreement with the low-Δ results quoted above. We checked that the parameters obtained for the high-Δ decompositions are also consistent with the HEXE data. Because of the fairly high statistical error, conclusive evidence as to the high-energy beam pattern of Cen X-3 was not obtained.

We further analyzed *Tenma* observations in three energy channels (Nagase 1989), shown in Figure 11. Pulse profile T2 exhibits a shoulder in the rising flank of the main peak, which develops into a small and pointed peak in pulse profile T3. A shoulder or peak at this position is absent both in the *OSO 8* and the *Ginga* data. There is an indication of a shoulder in the HEXE pulse profiles, though, and Howe et al. (1983) report an observation in the 12–34 keV energy range in which a shoulder is present at the respective phase.

We find that the pulse profile T1 without shoulder or secondary peak can be analyzed in excellent agreement with the results presented in § 4. The single-pole pulse profiles and the function of q are shown in Figure 12. Information on the statistical error of the *Tenma* data was not available to us. If we assume it to be fairly small, so that the shoulder and peak are highly significant, the two pulse profiles with shoulder or peak, respectively, are not amenable to this analysis. Asymmetric structures that are narrow and sharp to such a degree apparently must be intrinsic to the emission region.

A more detailed investigation of the secondary shoulder or maximum should be interesting, especially as this feature seems to be present only intermittently according to the observations by Howe et al. (1983), but such an investigation is beyond the scope of this paper.

5.3. *The Beam Pattern*

The beam pattern is determined by the local emission pattern of the emission region and by relativistic light

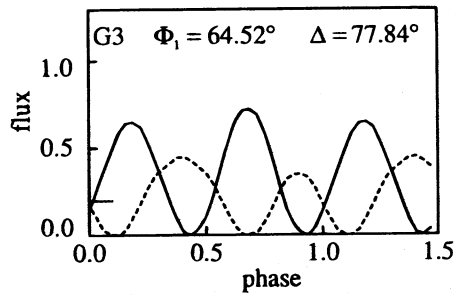

FIG. 10.—A decomposition of pulse profile G3 that is characteristic for decompositions in the region $60° \leq \Phi_1 \leq 80°$, $75° \leq \Delta \leq 90°$.

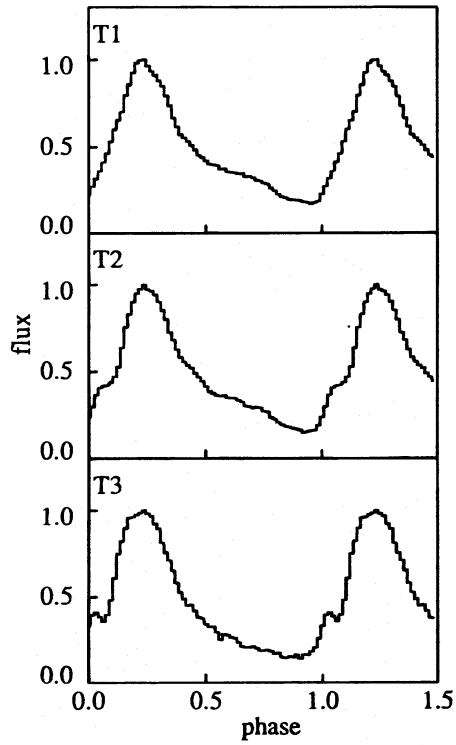

FIG. 11.—*Tenma* observation of Cen X-3 in the energy ranges 2–6 keV (T1), 6–10 keV (T2), and 10–20 keV (T3) (Nagase 1989).

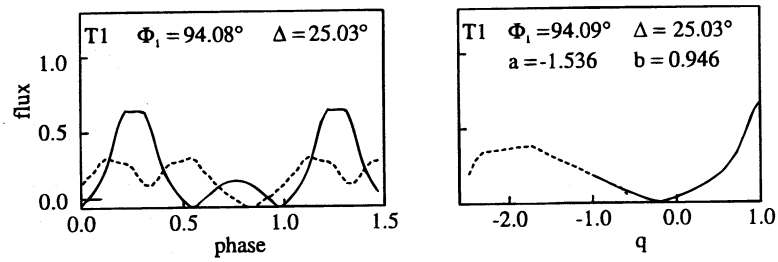

FIG. 12.—Decomposition of T1 and combined single-pole pulse profiles as a function of q. The parameters a and b are those of the high-Δ set of § 4.

deflection near the neutron star (Fig. 13). With an assumption about the ratio of the radius r_n of the neutron star and its Schwarzschild radius r_S, the beam pattern can give indications as to the local properties of the emission region by means of the intrinsic beam pattern and a constraint on the size of the emission region. In Figure 14, top row, the beam patterns G4 and G6 of Figure 7 are plotted as polar diagrams; the "plus" solutions are shown on the left, and the "minus" solutions are shown on the right. The beam patterns have been normalized so that the average flux per solid angle is unity. Figure 14, bottom row, shows polar diagrams of the intrinsic beam patterns of a point source on the neutron star surface that correspond to the G4 and G6 beam patterns for $r_n/r_s = 3.3$; see Figure 13 for the relation between intrinsic angle ϑ and asymptotic angle θ. The intrinsic beam patterns have also been normalized so that the average flux per solid angle is unity. The intrinsic beam patterns shown on the right have a minimum in the flux for all energies at $\vartheta \approx 90°$ and for $\vartheta > 90°$ all energy channels show a significant flux of photons; these photons have to come from regions in the plasma above the neutron star surface and/or from sections of the neutron star surface outside the pole. The beam pattern has been reconstructed in the range $56° \leq \theta \leq 123°$ and $57° \leq \theta \leq 124°$, respectively, for the "plus" solution and the "minus" solution. The condition that the emission region is visible up to $\theta = 124°$ provides a constraint on the size of the emission region. Figure 15 shows the minimum height of the emission region as a function of half-opening angle, $h_{\min}(\alpha)$ for $\theta_2 = 124°$ and different values of r_n/r_s. For a 1 $M_\odot$ neutron star with a radius of 10 km and $\alpha = 5°$, e.g., the height of the emission region would have to be $h \geq 13$ m. If the neutron star is so compact that $r_n/r_S \leq 2.7$, then there is no condition on the height h of the emitting point. For such a compact object, it is possible to observe an emitting point on the magnetic pole at $h = 0$ up to $\theta_2 = 124°$.

The analysis of the *Ginga* observations of Cen X-3 gives the beam pattern in seven energy channels as plotted in Figure 7. Another way to represent the same data is in the form of angle-dependent spectra as shown in Figure 16. Since we started out with normalized pulse profiles, absolute count rates are not available, and therefore we normalize the spectra also. This normalization is done by taking the ratio of each spectrum to the spectrum at the maximum of the beam pattern. Figure 16 shows the beam pattern of G1 as a function of θ_- (*top left*), where the range of θ_- has been divided into three regions, and spectra in regions I, II, and III. Normalization is with respect to the spectrum at $\theta_- = 69°$, marked by a box in the beam pattern plot, and spectra are plotted for those values of θ_- that are marked by arrows. We find that the spectra in regions I and II are very similar to the spectrum at maximum, since the normalized spectra are close to horizontal lines. However, the spectra in region III are clearly different. The normalized spectra are rising, i.e., the spectra in region III are harder than the spectrum at maximum.

The "plus" beam patterns plotted in Figure 7 (*upper abscissa*) and Figure 14 (*left*) show a declining flux for $\theta_+ \leq 75°$ which could be part of a pencil-beam pattern similar to those suggested by "slab" or "polar cap" models (Nagel 1981; Mészáros & Nagel 1985; Bulik et al. 1992, 1995; Pechenick, Ftaclas, & Cohen 1983). There is also a fan beam

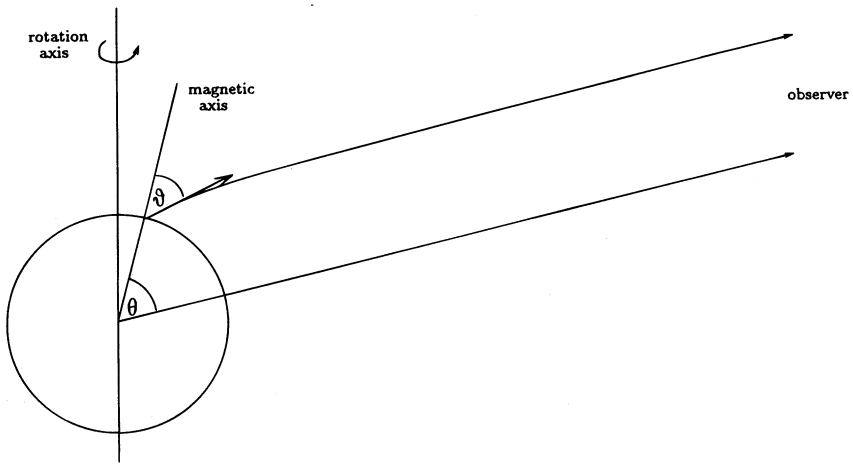

FIG. 13.—Photon emission from a point source on the magnetic pole at an emission angle ϑ with respect to the magnetic axis. An observer at infinity observes the radiation at an angle θ to the magnetic axis.

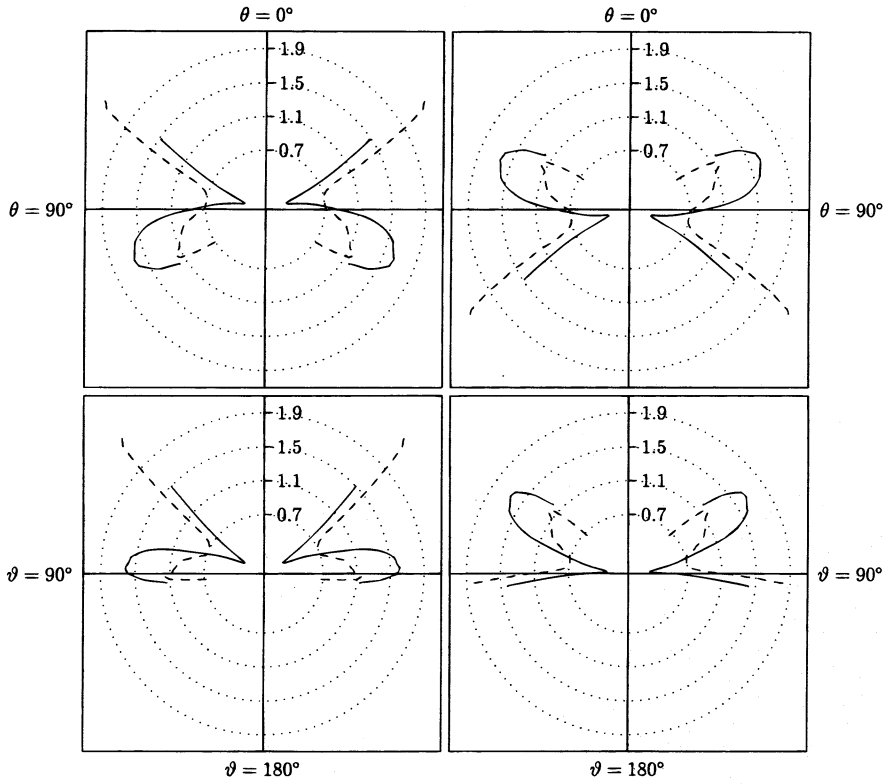

FIG. 14.—Polar diagrams of the reconstructed beam patterns (*top row*) and corresponding intrinsic beam patterns (*bottom row*) of G4 (*solid line*) and G6 (*dashed line*) for the "plus" solution (*left*) and the "minus" solution (*right*). The beam patterns have been normalized so that the average flux per solid angle is unity. The intrinsic beam patterns have been calculated for a neutron star with a ratio of 3.3 of its radius and Schwarzschild radius.

component at $\theta_+ > 90°$ which contains considerable flux and could be ascribed to relativistic light deflection near the neutron star (Riffert & Mészáros 1988). In the intrinsic beam pattern, the fan beam is approximately centered on $\vartheta_+ = 90°$. According to Figure 16, region III with the harder spectrum corresponds to $\theta_+ \leq 75°$, i.e., the pencil beam.

The "minus" beam patterns exhibit a peak around $\theta_- \approx 70°$, and emission appears to be suppressed at small θ_-, similar to what has been found in models that include scattering in the accretion stream or in a scattering atmosphere (Brainerd & Mészáros 1991; Sturner & Dermer 1994). Again there is considerable flux at $\theta_- > 90°$ which may be caused by relativistic light deflection. Here region III of

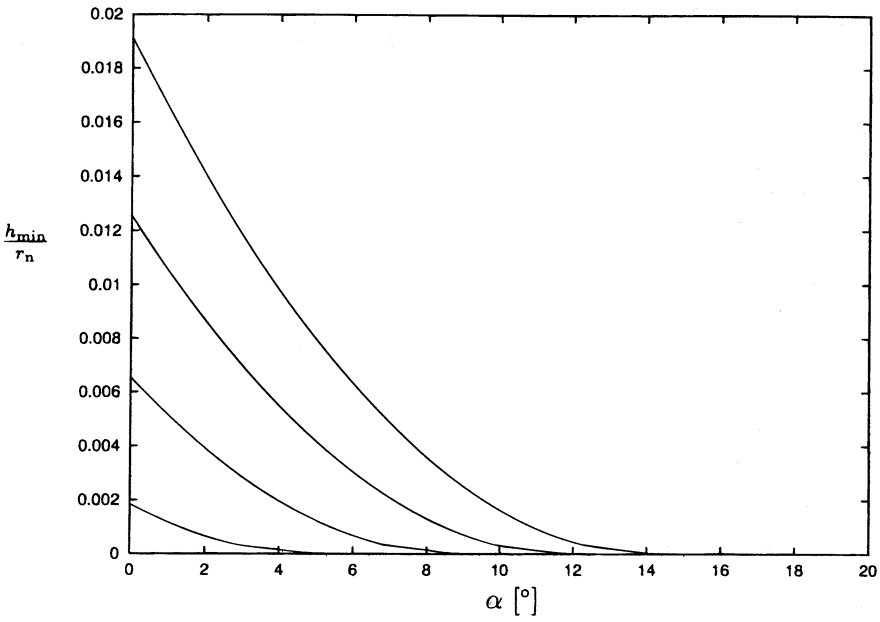

FIG. 15.—Minimum height h_{min} of the emission region of Cen X-3 for $\theta_2 = 124°$ as a function of half-opening angle α of the emission region for different values of the ratio of the radius and the Schwarzschild radius of the neutron star (3.9, 3.6, 3.3, and 3.0 from the top to bottom).

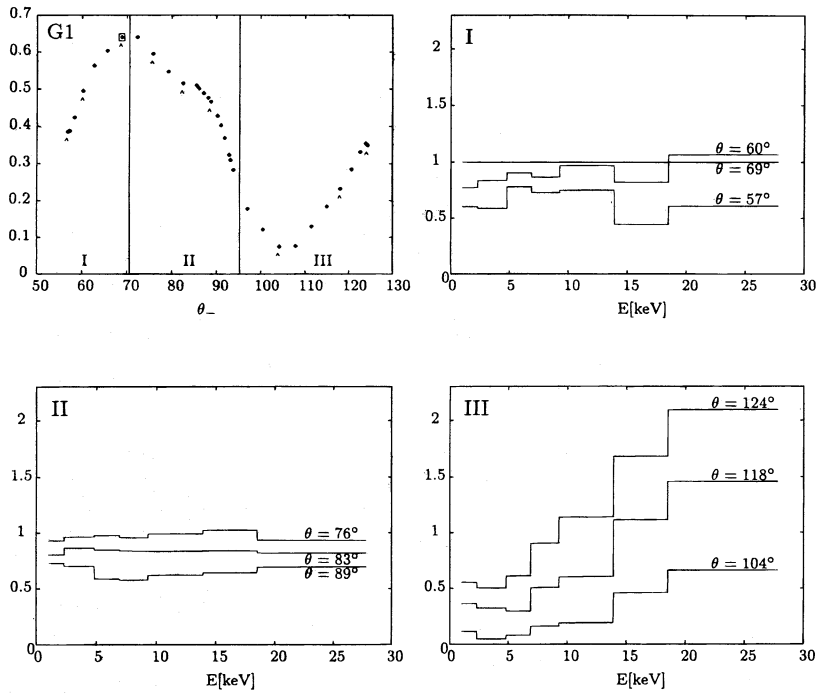

FIG. 16.—Normalized spectra obtained from the energy-dependent beam pattern of the *Ginga* pulse profiles (Fig. 7) *Top left*: Beam pattern of G1, where the θ_- range has been divided into three regions. Other plots: spectra in regions I, II, and III. Spectra are shown at the phases marked by arrows in the beam pattern plot and have been normalized by dividing them by the spectrum at maximum, indicated by the box in the beam pattern plot.

Figure 16 corresponds to $\theta_- \geq 105°$. In the intrinsic beam pattern, this means $\vartheta_- \geq 90°$, so that the harder spectrum is associated with radiation emitted "downward."

While there is not, to our knowledge, a model to date which would reproduce either the "plus" or the "minus" beam patterns as a whole, the main features of the beam patterns seem to be in qualitative agreement with the general properties expected from X-ray pulsar beam patterns.

An interpretation in terms of neutron star parameters or properties of the accretion stream would require detailed fits to model calculations. We should like to mention that fits to the reconstructed beam patterns involve fewer fit parameters than fits to the pulse profiles because the geometric parameters have already been determined. It might, however, be advisable to include Θ_O in the fit instead of equating Θ_O and the inclination.

The analysis of the energy dependent asymmetric pulse profile of Cen X-3 has shown that the data are compatible with the assumption that the asymmetry is caused by a distorted magnetic dipole field. The investigation of other sources may indicate to what extent this is a general feature of X-ray pulsar profiles.

We are grateful to the HEXE collaboration, in particular M. Kunz, Institut für Astronomie und Astrophysik–Abteilung Astronomie, Universität Tübingen, for kindly making the HEXE observations of Cen X-3 available to us.

This work has been supported by the Deutsche Forschungsgemeinschaft (DFG).

REFERENCES

Basko, M. M., Sunyaev, R. A. 1975, A&A, 42, 311
Brainerd, J. J., & Mészáros, P. 1991, ApJ, 369, 179
Bulik, T., Mészáros, P., Woo, J. W., Nagase, F., & Makishima, K. 1992, ApJ, 395, 564
Bulik, T., Riffert, H., Mészáros, P., Makishima, K., Mihara, T., & Thomas, B. 1995, ApJ, 444, 405
Dolan, J. F., Crannell, C. J., Dennis, B. R., Frost, K. J., & Orwig, L. E. 1984, ApJ, 278, 266
Giacconi, R., Gursky, H., Kellogg, E., Schreier, E., & Tananbaum, H. 1971, ApJ, 167, L67
Howe, S. K., Primini, F. A., Bautz, M. W., Lang, F. L., Levine, A. M., & Lewin, W. H. G. 1983, ApJ, 272, 678
Joss, P., & Rappaport, S. 1984, ARA&A, 22, 537
Kraus, U., Nollert, H.-P., Ruder, H., & Riffert, H. 1995, ApJ, 450, 763
Kunz, M. 1994, private communication
Leahy, D. A. 1991, MNRAS, 251, 203
Lieu, R., Venkatesan, D., & Mitani, K. 1984, ApJ, 282, 709
Mészáros, P., & Nagel, W. 1985, ApJ, 298, 147
Nagase, F. 1989, PASJ, 41, 1
Nagase, F., Corbet, R. H. D., Day, C. S. R., Inoue, H., Takeshima, T., & Yoshida, K. 1992, ApJ, 396, 147
Nagel, W. 1981, ApJ, 251, 278
Parmar, A. N., White, N. E., & Stella, L. 1989, ApJ, 338, 373
Pechenick, K. R., Ftaclas, C., & Cohen, J. M. 1983, ApJ, 274, 846
Priedhorsky, W. C., & Terrell, J. 1983, ApJ, 273, 709
Riffert, H., & Mészáros, P. 1988, ApJ, 325, 207
Riffert, H., Nollert, H.-P., Kraus, U., & Ruder, H. 1993, ApJ, 406, 195
Schreier, E. J., Swartz, K., Giacconi, R., Fabbiano, G., & Morin, J. 1976, ApJ, 204, 539
Sturner, S. J., & Dermer, C. D. 1994, A&A, 284, 161
Tuohy, I. R. 1976, MNRAS, 174, 45P
Ulmer, M. P. 1976, ApJ, 204, 548
van der Klis, M., Bonnet-Bidaud, J. M., & Robba, N. R. 1980, A&A, 88, 8
Wang, Y.-M., & Welter, G. L. 1981, A&A, 102, 97
White, N. E., Swank, J. H., & Holt, S. S. 1983, ApJ, 270, 711